

1 Article

2 Landscape classification with deep neural networks.

3 Daniel Buscombe ^{1,*} and Andrew C. Ritchie ²

4 ¹ Northern Arizona University, Flagstaff, AZ 86011, U.S.A; daniel.buscombe@nau.edu

5 ² U.S. Geological Survey, Santa Cruz, CA 95060, U.S.A; aritchie@usgs.gov

6 * Correspondence: daniel.buscombe@nau.edu; Tel.: +1-928-523-9280

7 Received: date; Accepted: date; Published: date

8 **Abstract:** The application of deep learning, specifically deep convolutional neural networks
9 (DCNNs), to the classification of remotely sensed imagery of natural landscapes has the potential
10 to greatly assist in the analysis and interpretation of geomorphic processes. However, the general
11 usefulness of deep learning applied to conventional photographic imagery at a landscape scale is,
12 at yet, largely unproven. If DCNN-based image classification is to gain wider application and
13 acceptance within the geoscience community, demonstrable successes need to be coupled with
14 accessible tools to retrain deep neural networks to discriminate landforms and land uses in
15 landscape imagery. Here, we present an efficient approach to train/apply DCNNs with/on sets of
16 photographic images, using a powerful graphical method, called a conditional random field (CRF),
17 to generate DCNN training and testing data using minimal manual supervision. We apply the
18 method to several sets of images of natural landscapes, acquired from satellites, aircraft, unmanned
19 aerial vehicles, and fixed camera installations. We synthesize our findings to examine the general
20 effectiveness of transfer learning to landscape scale image classification. Finally, we show how
21 DCNN predictions on small regions of images might be used in conjunction with a CRF for highly
22 accurate pixel-level classification of images.

23 **Keywords:** image classification; image segmentation; land use; land cover; landforms; deep
24 learning; machine learning; UAS; aerial imagery; remote sensing
25

26 1. Introduction

27 1.1. The growing use of image classification in the geosciences

28 There is a growing need for fully automated pixel-scale classification of large datasets of color
29 digital photographic imagery, to aid analysis and interpretation of natural landscapes and
30 geomorphic processes. The task of classifying natural objects and textures in images of landforms is
31 increasingly widespread in a wide variety of geomorphological research [1-7], providing impetus for
32 the development of completely automated methods to maximize speed and objectivity. The task of
33 labeling image pixels into discrete classes is called object class segmentation or semantic
34 segmentation, whereby an entire scene is parsed into object classes at a pixel level [8-9].

35 There is a growing trend in studies of coastal and fluvial systems for using automated methods
36 to extract information from time-series of imagery from fixed camera installations [10-16], UAVs [17-
37 19] and other aerial platforms [20]. Fixed camera installations are designed for generating time-series
38 of images for assessment of geomorphic change in dynamic environments. Many aerial imagery
39 datasets are collected for building digital terrain models and orthoimages using Structure-from-
40 Motion (SfM) photogrammetry [21,22]. Numerous complementary or alternative uses of such
41 imagery and elevation models for the purposes of geomorphic research include facies description
42 and grain size calculation [23,24], geomorphic and geologic mapping [25,26], vegetation structure
43 description [27,28], physical habitat quantification [29,30], and geomorphic/ecologic change detection
44 [31-33]. In this paper, we utilize and evaluate two emerging themes in computer vision research,

45 namely deep learning and structured prediction, that, when combined, are shown to be extremely
46 effective in application to pattern recognition and semantic segmentation of highly structured,
47 complex objects in images of natural scenes.

48 *1.2. Application of deep learning to landscape scale image classification*

49 Deep learning is the application of artificial neural networks with more than one hidden layer
50 to the task of learning and subsequently recognizing patterns in data [34,35]. A class of deep learning
51 algorithms called deep convolutional neural networks (DCNNs) are extremely powerful at image
52 recognition, resulting in a massive proliferation of their use [36,37], across almost all scientific
53 disciplines [38,39]. A major advantage to DCNNs over conventional machine learning approaches to
54 image classification is that they do not require so-called 'feature-engineering' or 'feature extraction',
55 which is the art of either transforming image data so that they are more amenable to a specific
56 machine-learning algorithm, or providing the algorithm more data by computing derivative
57 products from the imagery, such as rasters of texture or alternative colorspace [40,6,12]. In deep
58 learning, features are automatically learned from data using a general-purpose procedure. Another
59 reputed advantage is that DCNN performance generally improves with additional data, whereas
60 machine learning performance tends to plateau [41]. For these reasons, DCNN techniques will find
61 numerous applications where automated interpretation and quantification of natural landforms and
62 textures are used to investigate geomorphological questions.

63 However, many claims about the efficacy of DCNNs for image classification are largely based
64 upon analyses of conventional photographic imagery of familiar, mostly anthropogenic objects [42,6],
65 and it has not been demonstrated that this holds true for image classification of natural textures and
66 objects. Aside from the relatively large scale, images of natural landscapes collected for
67 geomorphological objectives tend to be taken from the air or at high vantage, with a nadir (vertical)
68 or oblique perspective. In contrast, images that make up many libraries upon which DCNNs are
69 trained and evaluated tend to be taken from ground level, with a horizontal perspective. In addition,
70 variations in lighting and weather greatly affect distributions of color, contrast and brightness; certain
71 land covers change appearance due to changing seasons (such as deciduous vegetation); and
72 geomorphic processes alter the appearance of land covers and landforms causing large intra-class
73 variation, for example, still/moving, clear, turbid, and aerated water. Finally, the distinction of certain
74 objects and features may be difficult against similar backgrounds, for example groundcover between
75 vegetation canopies.

76 The most popular DCNN architectures have been designed and trained on large generic image
77 libraries such as Imagenet [43], mostly developed as a result of international computer vision
78 competitions [44] and primarily for application to close-range imagery with small spatial footprints
79 [42], but more recently have been used for landform/land use classification tasks in large spatial
80 footprint imagery such as that used in satellite remote sensing [45-49]. These applications have
81 involved design and implementation of new or modified DCNN architectures, or relatively large
82 existing DCNN architectures, and have largely been limited to satellite imagery. Though powerful,
83 DCNNs are also computationally intensive to train and deploy, very data hungry (often requiring
84 millions of examples to train from scratch), and require expert knowledge to design and optimize.
85 Collectively, these issues may impede widespread adoption of these methods within the geoscience
86 community.

87 In this contribution, a primary objective is to examine the accuracy of DCNNs for oblique and
88 nadir conventional medium-range imagery. Another objective is to evaluate the smallest, most
89 lightweight existing DCNN models, retrained for specific land use/land cover purposes, with no
90 retraining from scratch and no modification or fine-tuning to the data. We utilize a concept known
91 as 'transfer learning', where a model trained on one task is re-purposed on a second related task [35].
92 Fortunately, several open-source DCNN architectures have been designed for general applicability
93 to the task of recognizing objects and features in non-specific photographic imagery. Here, we use
94 existing pre-trained DCNN models that are designed to be transferable for generic image recognition
95 tasks, which facilitates rapid DCNN training when developing classifiers for specific image sets.

96 Training is rapid because only the final layers in the DCNN need to be retrained to classify a specific
97 set of objects.

98 1.3. Pixel-scale image classification

99 Automated classification of pixels in digital photographic images involves predicting labels, y ,
100 from observations of features, x , which are derived from relative measures of color in red, green and
101 blue spectral bands in imagery. In the geosciences, the labels of interest naturally depend on the
102 application but may be almost any type of surface land cover (such as specific sediment, landforms,
103 geological features, vegetation type and coverage, water bodies, etc) or description of land use
104 (rangeland, cultivated land, urbanized land, etc). The relationships between x and y are complex and
105 non-unique, because the labels we assign depend nonlinearly on observed features, as well as on each
106 other. For example, neighboring regions in an image tend to have similar labels (i.e. they are spatially
107 autocorrelated). Depending on the location and orientation of the camera relative to the scene, labels
108 may be preferentially located. Some pairs of labels (e.g. ocean and beach sand) are more likely to be
109 proximal than others (e.g. ocean and arable land).

110 A natural way to represent the manner in which labels depend on each other is provided by
111 graphical models [50] where input variables (in the present case, image pixels and their associated
112 labels) are mapped onto a graph consisting of nodes, and edges between the nodes describe the
113 conditional dependence between the nodes. Whereas a discrete classifier can predict a label without
114 considering neighboring pixels, graphical models can take this spatial context into account, which
115 makes them very powerful for classifying data with large spatial structure, such as images. Much
116 work in learning with graphical models has focused on generative models that explicitly attempt to
117 model a joint probability distribution $P(x,y)$ over inputs, x , and outputs, y . However, this approach
118 has important limitations for image classification where the dimensionality of x is potentially very
119 large, and the features may have complex dependencies, such as the dependencies or correlations
120 between multiple metrics derived from images. In such cases, modeling the dependencies among x
121 is difficult and leads to unmanageable models, but ignoring them can lead to poor classifications.

122 A solution to this problem is a discriminative approach, similar to that taken in classifiers such
123 as logistic regression. The conditional distribution $P(y|x)$ is modeled directly, which is all that is
124 required for classification. Dependencies that involve only variables in x play no role in $P(y|x)$, so an
125 accurate conditional model can have much simpler structure than a joint model, $P(x,y)$. The posterior
126 probabilities of each label are modeled directly, so no attempt is made to capture the distributions
127 over x , and there is no need to model the correlations between them. Therefore, there is no need to
128 specify an underlying prior statistical model, and the conditional independence assumption of a pixel
129 value given a label, commonly used by generative models, can be relaxed.

130 This is the approach taken by conditional random fields (CRFs), which are a combination of
131 classification and graphical modeling known as structured prediction [51,50]. They combine the
132 ability of graphical models to compactly model multivariate data (the continuum of land cover and
133 land use labels) with the ability of classification methods to leverage large sets of input features,
134 derived from imagery, to perform prediction. In CRFs based on 'local' connectivity, nodes connect
135 adjacent pixels in x [51,52], whereas in the fully connected definition, each node is linked to every
136 other [53,54]. CRFs have recently been used extensively for task-specific predictions such as in
137 photographic image segmentation [55,56,42] where, typically, an algorithm estimates labels for
138 sparse (i.e. non-contiguous) regions (i.e. supra-pixel) of the image. The CRF uses these labels in
139 conjunction with the underlying features (derived from a photograph), to draw decision boundaries
140 for each label, resulting in a highly accurate pixel-level labeled image [54,42].

141 1.4. Paper purpose, scope, and outline

142 In summary, this paper evaluates the utility of DCNNs for both image recognition and semantic
143 segmentation of images of natural landscapes. Whereas previous studies have demonstrated the
144 effectiveness of DCNNs for classification of features in satellite imagery, we specifically use examples
145 of high-vantage and nadir imagery that are commonly collected during geomorphic studies and in

146 response to disasters/natural hazards. In addition, whereas many previous studies have utilized
 147 DCNNs either specifically designed to recognize landforms, land cover or land use, or trained
 148 existing DCNN architectures from scratch using a specific dataset, the comparatively simple
 149 approach taken here is to repurpose an existing DCNN to a specific task. Previous studies have
 150 tended to use relatively large DCNN architectures, whereas here we use the comparatively small,
 151 very fast MobileNetV2 framework. Further, we demonstrate how structured prediction using a fully
 152 connected CRF can be used in a semi-supervised manner to efficiently generate ground truth label
 153 imagery and DCNN training libraries. Finally, we propose a hybrid method for accurate semantic
 154 segmentation based on combining 1) the recognition capacity of DCNNs to classify small regions in
 155 imagery, and 2) the fine grained localization of fully connected CRFs for pixel-level classification.

156 The rest of the paper is organized as follows. First, we outline the CRF method, and its use in
 157 the generation of ground truth label images and DCNN training libraries. Then we detail the transfer
 158 learning approach taken to DCNN model repurposing, and how DCNN model predictions on small
 159 regions of an image may be used in conjunction with a CRF for semantic classification. Four datasets
 160 for image classification are introduced. The first is a large satellite dataset consisting of various
 161 natural land covers and landforms, and the final three are from high-vantage or aerial imagery. Those
 162 three are also used for semantic classification. In either case, some data is used for training the DCNN,
 163 and some for testing classification skill (out-of-calibration validation). For each of the datasets, we
 164 evaluate the ability of the DCNN to classify regions of images or whole images correctly. The skill of
 165 the semantic segmentation is assessed. Finally, we discuss the utility of these findings and broader
 166 application of these methods for geomorphic research, before conclusions are drawn.

167 2. Materials and Methods

168 2.1. Fully connected Conditional Random Field

169 A conditional random field (CRF) is an undirected graphical model that we use here to
 170 probabilistically predict pixel labels based on weak supervision, which could be manual label
 171 annotations or classification outputs from discrete regions of an image based on outputs from a
 172 trained DCNN. Image features x and labels y are mapped to graphs, whereby each node is connected
 173 to an edge to its neighbors according to a connectivity rule. Linking each node of the graph created
 174 from x to every other node enables modeling of the long-range spatial connections within the data
 175 by considering both proximal and distal pairs of grid nodes, resulting in refined labeling at
 176 boundaries and transitions between different label classes. We use the fully connected CRF approach
 177 detailed in [54], which is summarized briefly below. The probability of a labeling y given an image-
 178 derived feature, x , is

$$P(y|x, \theta) = \frac{1}{Z(x, \theta)} \exp(-E(y|x, \theta)) \quad (1)$$

179 where θ is a set of hyperparameters, Z is a normalization constant, and E is an energy function that
 180 is minimized, obtained by

$$E(y|x, \theta) = \sum_i \psi_i(y_i, x_i | \theta) + \sum_{i < j} \psi_{ij}(y_i, y_j, f_i, f_j | \theta) \quad (2)$$

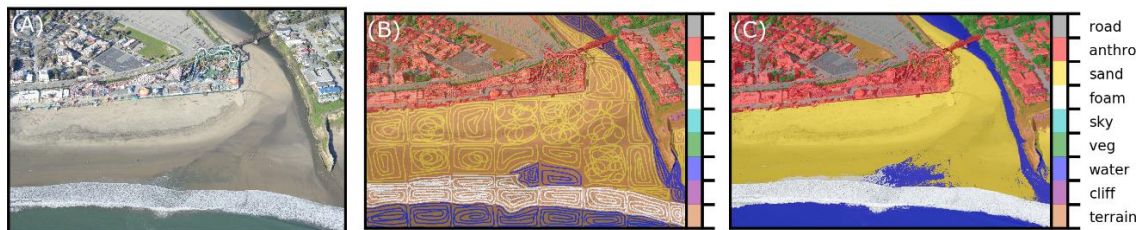
181 where i and j are pixel locations in the horizontal (row) and vertical (column) dimensions. The
 182 vectors f_i and f_j are features created from x_i and x_j and are functions of both relative position and
 183 intensity of the image pixels. The term ψ_i indicate so-called 'unary potentials', which depend on the
 184 label at a single pixel location (i) of the image, whereas 'pairwise potentials', ψ_{ij} , depend on the labels
 185 at a pair of separated pixel locations (i and j) on the image. The unary potentials represent the cost of
 186 assigning label y_i to grid node i . In this paper, unary potentials are defined either through sparse
 187 manual annotation or automated classification using DCNN outputs. The pairwise potentials are the
 188 cost of simultaneously assigning label y_i to grid node i and y_j to grid node j , and are computed
 189 using image feature extraction, defined by:

$$\psi_{ij}(y_i, y_j, f_i, f_j | \theta) = \Lambda(y_i, y_j | \theta) \sum_{l=1}^L k^l(f_i^l, f_j^l) \quad (3)$$

190 where $l = 1:L$ are the number of features derived from x , and where the function Λ quantifies label
 191 'compatibility', by imposing a penalty for nearby similar grid nodes that are assigned different labels.
 192 Each k^l is the sum of two Gaussian kernel functions that determines the similarity between
 193 connected grid nodes by means of a given feature f^l :
 194

$$k^l(f_i^l, f_j^l) = \exp\left(-\frac{|p_j - p_i|^2}{2\theta_\alpha^2} - \frac{|x_j - x_i|^2}{2\theta_\beta^2}\right) + \exp\left(-\frac{|p_j - p_i|^2}{2\theta_\gamma^2}\right) \quad (4)$$

195 The first Gaussian quantifies the observation that nearby pixels, with a distance controlled by
 196 θ_α (standard deviation for the location component of the color-dependent term), with similar color,
 197 with similarity controlled by θ_β (standard deviation for the color component of the color-dependent
 198 term), are likely to be in the same class. The second Gaussian is a 'smoothness' kernel that removes
 199 small isolated label regions, according to θ_γ , the standard deviation for the location component.
 200 This penalizes small pieces of segmentation that are spatially isolated, enforcing more spatially
 201 consistent classification. Hyperparameter θ_β controls the degree of allowable similarity in image
 202 features between CRF graph nodes. Relatively large θ_β means image features with relatively large
 203 differences in intensity may be assigned the same class label. Similarly, a relatively large θ_α means
 204 image pixels separated by a relatively large distance may be assigned the same class label.
 205



206 **Figure 1.** Application of the semi-supervised CRF at Seabright beach for generation of DCNN training
 207 tiles and ground-truth labeled images. From left to right, (A) the input image, (B) the hand-annotated
 208 sparse labels, and (C) the resulting CRF-predicted pixelwise labeled image.

209 2.2. Generating DCNN training libraries

210 We developed a user-interactive program that segments an image into smaller chunks, the size
 211 of which is defined by the user. On each chunk, cycling through a pre-defined set of classes, the user
 212 is prompted to draw (using the cursor) example regions of the image that correspond to each label.
 213 Unary potentials are derived from these manual on-screen image annotations. Using this
 214 information, the CRF algorithm estimates the class of each pixel in the image (Figure 1). Finally, the
 215 image is divided up into tiles of a specified size, T . If the proportion of pixels within the tile is greater
 216 than a specified amount, P_{class} , then the tile is written to a file in a folder denoting its class. This
 217 simultaneously and efficiently generates both ground-truth label imagery (to evaluate classification
 218 performance) and sets of data suitable for training a DCNN. A single photograph typically takes 5-
 219 30 minutes to process with this method, so all the data required to retrain a DCNN (see section below)
 220 may take only up to a few hours to generate. CRF inference time depends primarily on image
 221 complexity and size, but also secondarily affected by the number and spatial heterogeneity of class
 222 labels.

223 2.3. Retraining a deep neural network (transfer learning)

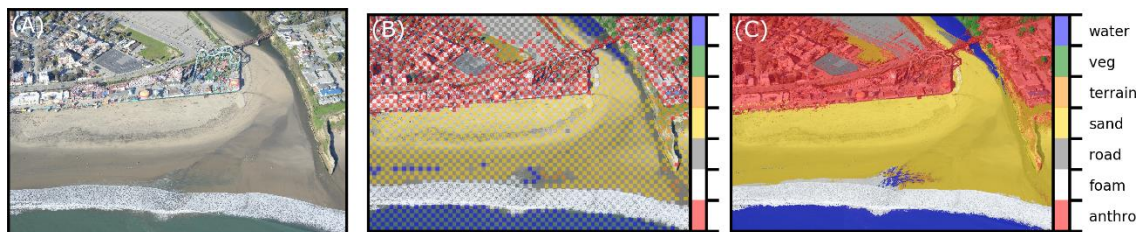
224 Among many suitable popular and open-source frameworks for image classification using deep
 225 convolutional neural networks, we chose MobileNetV2 [57] because it is relatively small and efficient
 226 (computationally faster to train and execute) compared to many competing architectures designed to
 227 be transferable for generic image recognition tasks, such as Inception [58], Resnet [59], and NASnet
 228 [60], and it is smaller and more accurate than MobileNetV1 [61]. It also is pretrained for various tile
 229 sizes (image windows with horizontal and vertical dimensions of 96, 128, 192, and 224 pixels) which
 230 allows us to evaluate that effect on classifications. However, all of the aforementioned models are
 231 implemented within TensorFlow-Hub [62], which is a library specifically designed for reusing pre-
 232 trained TensorFlow [63] models on new tasks.

233 For all datasets, we only used tiles (in the training and evaluation) where 90% of the tile pixels
 234 were classified as a single class (that is, $P_{class} > 0.9$). This avoided including tiles depicting mixed land
 235 cover/use classes. We chose tile sizes of $T = 96 \times 96$ pixels and $T = 224 \times 224$ pixels, which is the full range
 236 available for MobileNets, in order to compare the effect of tile size. All model training was carried
 237 out in Python using TensorFlow library version 1.7.0 and TensorFlow-hub version 0.1.0. For each
 238 dataset, model training parameters (1000 training steps, and a learning rate of 0.01) were kept
 239 constant, but not necessarily optimal. For most datasets, there are relatively small numbers of very
 240 general classes (water, vegetation, etc.), which in some ways is a more difficult classification task than
 241 much more specific classes, owing to the greater within-class variability to be expected from having
 242 broadly defined categories.

243 Each training and testing image tile is normalized against varying illumination and contrast,
 244 which greatly aids transferability of the trained DCNN model. A normalized image (X') is calculated
 245 from a non-normalized image (X) using

$$X' = \frac{X - \mu}{\sigma} \quad (5)$$

where μ and σ are mean and standard deviation, respectively [47]. We chose to scale every tile
 by a maximum possible standard deviation (for an 8-bit image) by using $\sigma = 255$. For each tile, μ
 was chosen as the mean across all three bands for that tile. This procedure could be optimized
 for a given dataset but in our study the effects of varying values of σ were minimal.



246 **Figure 2.** Application of the unsupervised CRF for pixelwise classification, based on unary potentials
 247 of regions of the image classified using a DCNN. Example comes from Seabright beach. From left to
 248 right, (A) the input image, (B) the DCNN-estimated sparse labels, and (C) the resulting CRF-predicted
 249 pixelwise labeled image.

250 2.4. CRF-based semantic segmentation

251 We developed a method that harnesses the classification power of the DCNN, with the
 252 discriminative capabilities of the CRF, for pixel-scale semantic segmentation of imagery. An input
 253 image is windowed into small regions of pixels, the size of which is dictated by the size of the tile
 254 used in the DCNN training (here, $T = 96 \times 96$ or $T = 224 \times 224$ pixels). Some windows, ideally with an even
 255 spatial distribution across the image, are classified with a trained DCNN. Collectively, these
 256 predictions serve as unary potentials (known labels) for a CRF to build a probabilistic model for
 257 pixelwise classification given the known labels and the underlying image (Figure 2).

258 Adjustable parameters are: 1) the proportion of the image to estimate unary potentials for
 259 (controlled by both T and the number/spacing of tiles), and 2) a threshold probability, P_{thres} , larger
 260 than which a DCNN classification was used in the CRF. Across each dataset, we found that using

261 50% of the image as unary potentials, and $P_{thres} = 0.5$, resulted in good performance. CRF
 262 hyperparameters were also held constant across all datasets. We found that good performance across
 263 all datasets was achieved using $\theta_\alpha = 60$, $\theta_\beta = 5$, and $\theta_\gamma = 60$. Holding all of these parameters constant
 264 facilitates comparison of the general success of the proposed method. However, it should be noted
 265 that accuracy could be further improved for individual datasets by optimizing the parameters for
 266 those specific data. This could be achieved by minimizing the discrepancy between ground truth
 267 label images and model-generated estimates using a validation dataset.

268 2.5. Metrics to assess classification skill

269 Standard metrics of precision, P , recall, R , accuracy, A , and F1 score, F , are used to assess
 270 classification of image regions and pixels. Where TP , TN , FP , and FN are, respectively, the frequencies
 271 of true positives, true negatives, false positives, and false negatives:

$$P = \frac{TP}{TP + FP} \quad (6)$$

272

$$R = \frac{TP}{TP + FN} \quad (7)$$

273

$$A = \frac{TP + TN}{TP + TN + FP + FN} \quad (8)$$

274

$$F = 2 \cdot \frac{P \cdot R}{P + R} \quad (9)$$

275

276 True positives are image regions/pixels correctly classified as belonging to a certain class by the
 277 model, while true negatives are correctly classified as not belonging to a certain class. False negatives
 278 are regions/pixels incorrectly classified as not belonging to a certain class, and false positives are those
 279 regions/pixels incorrectly classified as belonging to a certain class. Precision and recall are useful
 280 where the number of observations belonging to one class is significantly lower than those belonging
 281 to the other classes. These metrics are therefore used in evaluation of pixelwise segmentations, where
 282 the number of pixels corresponding to each class vary considerably. The F1 score is an equal
 283 weighting of the recall and precision and quantifies how well the model performs in general. Recall
 284 is a measure of the ability to detect the occurrence of a class, which is a given landform, land use or
 285 land cover.

286 A 'confusion matrix', which is the matrix of normalized correspondences between true and
 287 estimated labels, is a convenient way to visualize model skill. A perfect correspondence between true
 288 and estimated labels is scored 1.0 along the diagonal elements of the matrix. Misclassifications are
 289 readily identified as off-diagonal elements. Systematic misclassifications are recognized as off-
 290 diagonal elements with large magnitudes. Full confusion matrices for each test and dataset are
 291 provided as Supplemental Data 2.

292



293 **Figure 3.** Example tiles from NWPU dataset. Classes, from left to right, are beach, chaparral, desert,
294 forest, island, lake, meadow, mountain, river, sea ice, and wetland.

295 2.6. Data

296 The chosen datasets encompass a variety of shoreline environments (coastal, fluvial and
297 lacustrine) and collection platforms (oblique stationary cameras, oblique aircraft, nadir UAV, and
298 nadir satellite).

299 2.6.1. NWPU-RESISC45

300 To evaluate the MobileNetV2 DCNN with a conventional satellite-derived land use/land cover
301 dataset, we chose the NWPU-RESISC45, which is a publicly available benchmark for REmote Sensing
302 Image Scene Classification (RESISC), created by Northwestern Polytechnical University (NWPU).
303 The entire dataset, described by [6], contains 31,500 high-resolution images from Google Earth
304 imagery, in 45 scene classes with 700 images in each class. The majority of those classes are
305 urban/anthropogenic. We chose to use a subset of 11 classes corresponding to natural landforms and
306 land cover (Figure 3), namely: beach, chaparral, desert, forest, island, lake, meadow, mountain, river,
307 sea ice, and wetland. All images are 256x256 pixels. We randomly chose 350 images from each class
308 for DCNN training, and 350 for testing.
309



310 **Figure 4.** Example tiles from Seabright beach. Classes, from left to right, are anthropogenic/buildings,
311 foam, road/pavement, sand, other natural terrain, vegetation, and water.

312 2.6.2. Seabright beach, CA.

313 The dataset consists of 13 images of the shoreline at Seabright, Santa Cruz, CA. Images were
314 collected from a fixed-wing aircraft in February 2016, of which a random subset of seven were used
315 for training, and six for testing (Supplemental data S1A and S1B). Training and testing tiles were
316 generated for seven classes (Table A1 and Figures 2, 3, and 4).



317 **Figure 5.** Example tiles from Lake Ontario shoreline. Classes, from left to right, are
318 anthropogenic/buildings, sediment, other natural terrain, vegetation, and water.

319 2.6.3. Lake Ontario, NY.

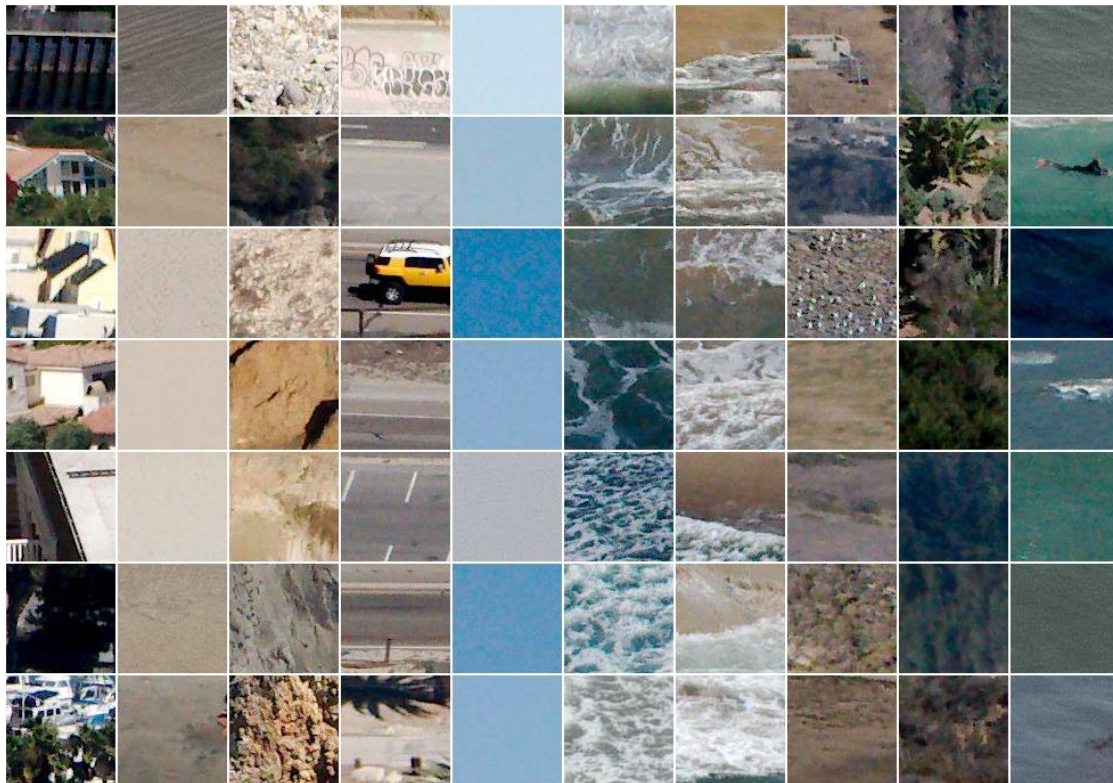
320 The dataset consists of 48 images obtained in July 2017 from a Ricoh GRII camera mounted to a
321 3DR Solo quadcopter, a small unmanned aerial system (UAS), flying 80-100 meters above ground
322 level in the vicinity of Braddock Bay, New York, on the shores of southern Lake Ontario [64]. A
323 random subset of 24 were used for training, and 24 for testing (Supplemental data S1C and S1D).
324 Training and testing tiles were generated for five classes (Table A2 and Figure 5).



325 **Figure 6.** Example tiles from Grand Canyon. Classes, from left to right, are rock/scree, sand,
326 vegetation, and water.

327 2.6.4. Grand Canyon, AZ.

328 The dataset consists of 14 images collected from a stationary autonomous camera systems
329 monitoring eddy sandbars along the Colorado River in Grand Canyon. The camera system, sites and
330 imagery is described in [16]. Imagery came from various seasons and river flow levels, and sites differ
331 considerably in terms of bedrock geology, riparian vegetation, sunlight/shade, and water turbidity.
332 One image from each of seven sites were used for training, and one from each those of same seven
333 sites were used for testing (Supplemental data S1E and S1F). Training and testing tiles were generated
334 for four classes (Table A3 and Figure 6).



335 **Figure 7.** Example tiles from CCRP dataset. Classes, from left to right, are buildings/anthropogenic,
 336 beach, cliff, road, sky, surf/foam, swash, other natural terrain, vegetation, and water.

337 2.6.5. California Coastal Records (CCRP).

338 The dataset consists of a sample of 75 images from the California Coastal Records Project (CCRP)
 339 [65], of which 45 were used for training, and 30 for testing (Supplemental data S1G and S1H). The
 340 photographs were taken over several years and times of the year, from sites all along the California
 341 coast, with a handheld digital single-lens reflex camera from a helicopter flying at approximately 50–
 342 600 m elevation [20]. The set includes a very wide range of coastal environments, at very oblique
 343 angles, with a corresponding very large horizontal footprint. Training and testing tiles were
 344 generated for ten classes (Table A4 and Figure 7).

345 **Table 1.** Out-of-calibration whole tile classification accuracies and F1 scores for each dataset and tile
 346 size.

Dataset	T = 96		T = 224	
	Mean accuracy	Mean F1 score	Mean accuracy	Mean F1 score
1. NWPU	87%	93%	89%	94%
2. Seabright	94%	97%	96%	97%
3. Ontario	83%	91%	96%	98%
4. Grand Canyon	92%	96%	94%	97%
5. CCRP	79%	88%	84%	91%

347 **3. Results**

348 **Table 2.** Mean out-of-calibration whole tile classification accuracies (%), per class, for each of the
 349 non-satellite datasets (T=96 / T=224).

	Seabright	Ontario	Grand Canyon	CCRP
Sediment/sand	93 / 98	76 / 93	94 / 89	91 / 89
Terrain/rock	91 / 91	78 / 91	89 / 95	84 / 78
Cliff				69 / 86
Vegetation	89 / 95	96 / 98	94 / 90	49 / 74
Water	99 / 98	94 / 97	92 / 99	92 / 91
Anthropogenic	95 / 98	72 / 94		79 / 85
Foam/Surf	97 / 96			72 / 81
Swash				79 / 79
Road	96 / 98			85 / 83
Sky				90 / 97

350

351 *3.1. Whole image tile classification accuracy*

352 With no fine tuning of model parameters, we achieved average classification accuracies of between
 353 91 and 98% (F1 scores) across five datasets with $T=224$ tiles, and between 88% and 97% with $T=96$ tiles
 354 (Table 1). Over 26 individual land cover/use classes (Table 2) in four datasets, average classification
 355 accuracies ranged between 49 and 99%. Confusion matrices (Supplemental 2, Figures S2A through S2E)
 356 for all classes reveal that most mis-classifications occur between similar groupings, for example swash
 357 and surf, and roads and buildings/anthropogenic. Confusion matrices therefore provide the means with
 358 which to identify which classes to group, if necessary, to achieve even greater overall classification
 359 accuracies. Only for certain data and classes did the distinction between $T=96$ and $T=224$ tiles make a
 360 significant difference, particularly for the Lake Ontario data where classifications were systematically
 361 better using $T=224$.

362 *3.2. Pixel classification accuracy*

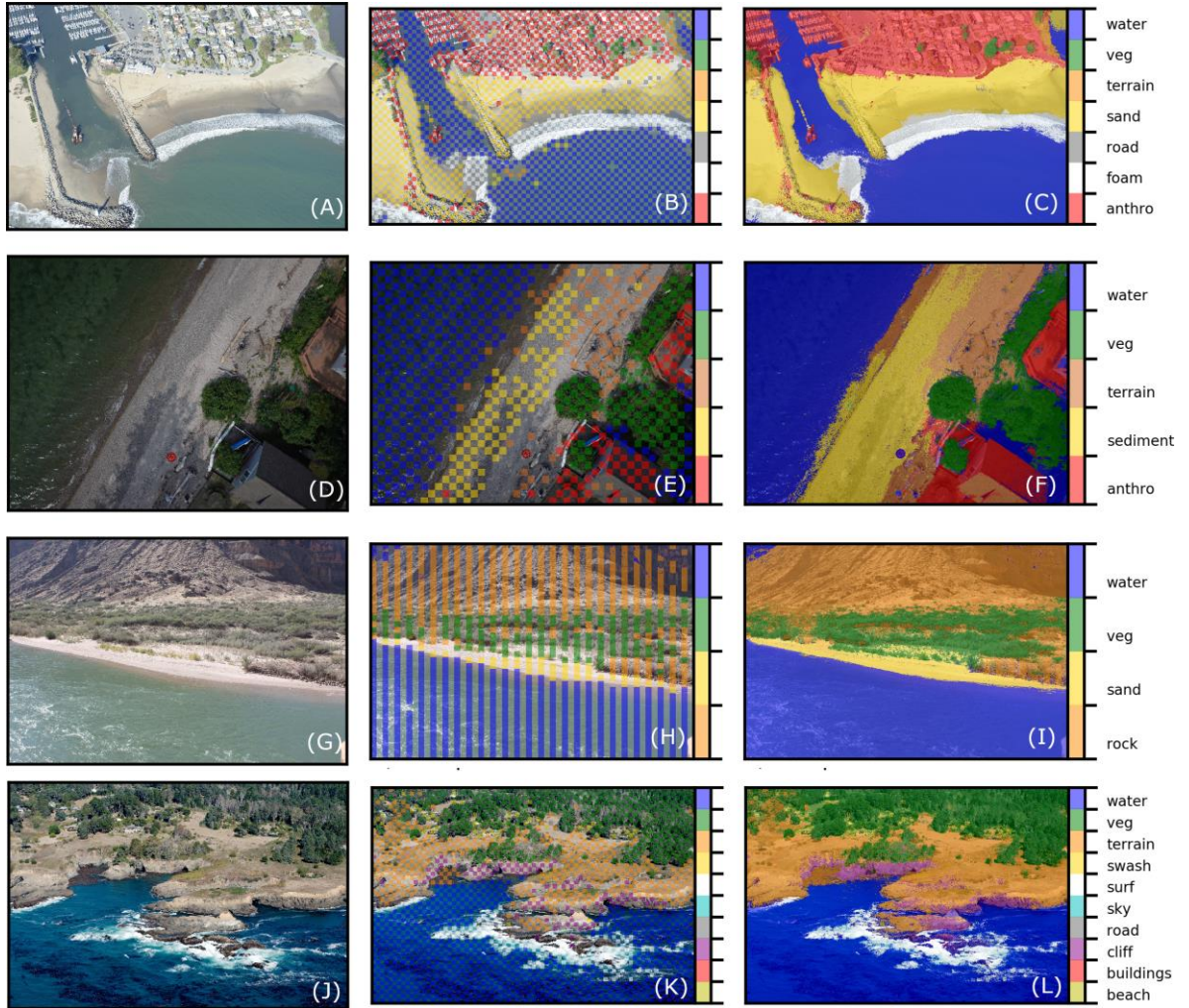
363 With no fine tuning of model parameters, we achieved average pixelwise classification
 364 accuracies of between 70 and 78% (F1 scores, Table 3) across four datasets, based on CRF modeling
 365 of sparse DCNN predictions with $T=96$ tiles (Figure 8). Classification accuracy for a given feature was
 366 found to be strongly related to size of that feature (Figure 9). For those land cover/uses that are much
 367 greater in size than a 96×96 pixel tile, average pixelwise F scores were much higher, ranging from 86
 368 to 90 %. Confusion matrices (Supplemental A, Figures S2F through S2I) again show how mis-
 369 classifications only systematically tend to occur between pairs of the most similar classes.

370 **Table 3.** Mean out-of-calibration P/R/F/A (all %) per class for pixelwise classifications using each of
 371 the non-satellite datasets ($T=96$).

	Seabright	Ontario	Grand Canyon	CCRP
Sediment/sand	98/92/95/92	72/72/74/67	76/79/80/78	84/90/86/78
Terrain/rock	44/51/46/50	32/32/30/41	80/97/87/96	47/86/54/75
Cliff				72/91/66/74
Vegetation	63/41/48/42	90/93/89/91	92/31/46/43	94/40/48/26
Water	95/92/93/91	95/95/95/89	94/92/93/94	93/88/86/79
Anthropogenic	87/95/90/94	78/59/64/55		85/70/76/71
Foam/Surf	87/93/90/94			93/74/73/70
Swash				42/40/48/27

Road	86/81/83/79			35/70/35/64
Sky				95/97/94/82
Average:	80/78/78/77	73/70/70/69	86/75/77/78	74/75/67/65

372



373
374
375

Figure 8. Example images (left column), DCNN-derived unary potentials (middle column), and CRF-derived pixelwise semantic segmentation (right column) for each of the four datasets, from top to bottom, Seabright, Lake Ontario, Grand Canyon, and CCRP.

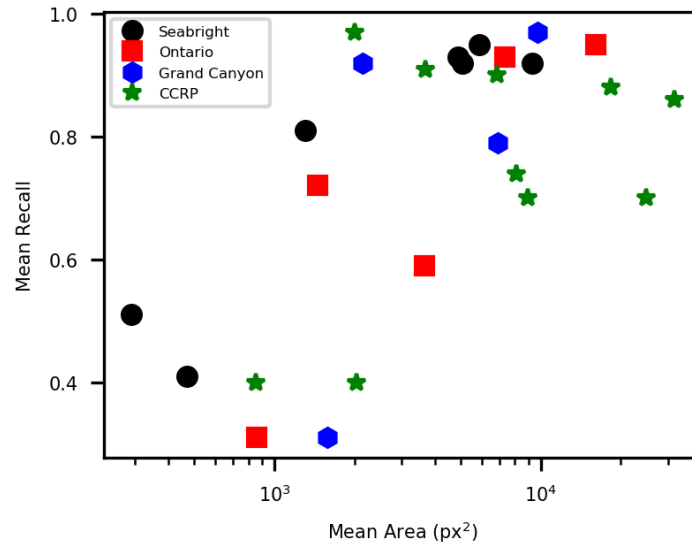


Figure 9. Average recall versus average area (in square pixels) of classes.

376

377

378

379 4. Discussion

380 Deep learning has revolutionized the field of image classification in recent years [36-39,42-49].
 381 However, the general usefulness of deep learning applied to conventional photographic imagery at
 382 a landscape scale is, at yet, largely unproven. Here, similar to previous workers who have
 383 demonstrated the ability of DCNNs for classification of land use/cover in long-range remotely sensed
 384 imagery from satellites [6,9,45-49], we show that DCNNs are powerful tools for classifying landforms
 385 and land cover in medium-range imagery acquired from UAS, aerial, and ground-based platforms.
 386 Further, we show that the smallest and most computationally efficient widely available DCNN
 387 architecture, MobilenetsV2, classifies land use/cover with comparable accuracies to larger, slower,
 388 DCNN models such as AlexNet [66,45,6], VGGNet [67,45,6], GoogLeNet [6,68,69], or custom-
 389 designed DCNNs [9,46,47]. Here, we deliberately chose a standard set of model parameters, and
 390 achieved reasonable pixel-scale classifications across all classes, but even greater accuracy is likely
 391 attainable with a model fine-tuned to a particular dataset [6].

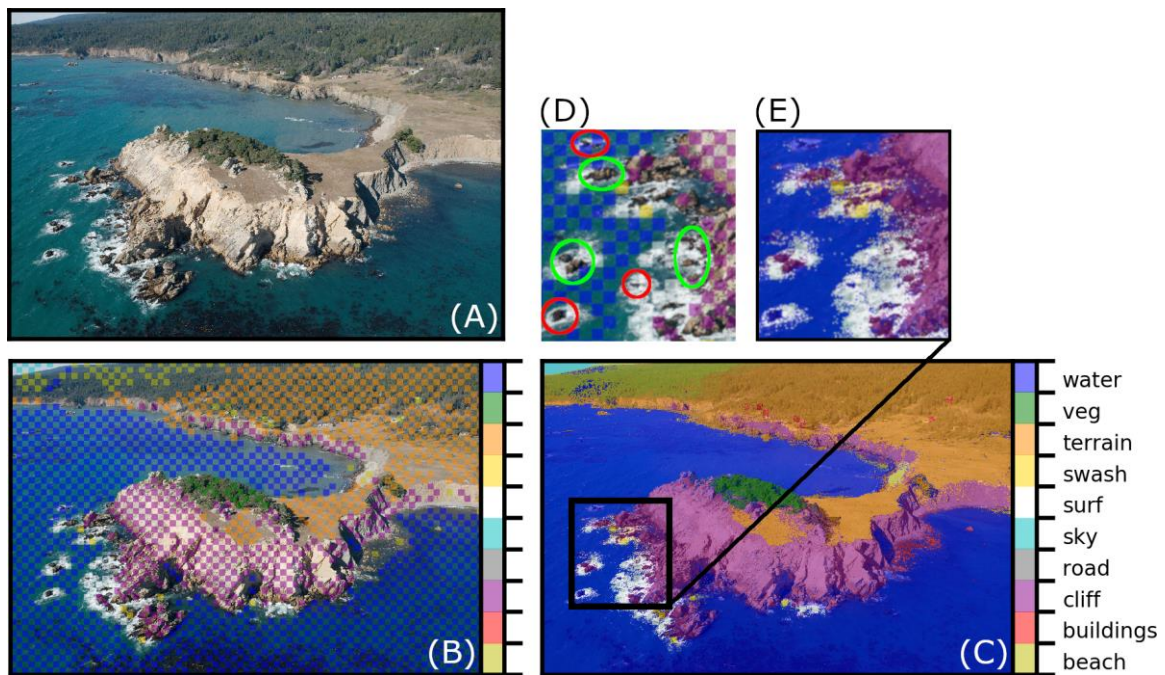
392 In remote sensing, the acquisition of pixel-level reference/label data is time-consuming and
 393 limiting [46], so acquiring a suitably large dataset for training DCNN is often a significant challenge.
 394 Therefore most studies that use pixel-level classifications only use a few hundred reference points
 395 [70,71]. We have suggested a new method for generating pixel-level labeled imagery for use in
 396 developing and evaluating classifications (DCNN-based and others), based on manual on-screen
 397 annotations in combination with a fully connected conditional random field (CRF, Figure 1). This, in
 398 conjunction with transfer learning and small, efficient DCNNs, provides the means to rapidly train a
 399 DCNN with a small dataset. In turn, this facilitates the rapid assessment of the general utility of
 400 DCNN architectures for a given classification problem, as well as the means to fine-tune a feature
 401 class or classes iteratively based on classification mismatches. The workflow presented here can be
 402 used to quickly assess the potential of a small DCNN like MobilenetV2 for a specific classification
 403 task. This ‘prototyping’ stage can also be used to assess classes that should be grouped, or split,
 404 depending on analysis of confusion matrices such as presented in Supplemental 2, Figures S2A through
 405 S2E. If promising, larger models such as Resnet [59] or NASnet [60] could be used, within the same
 406 framework provided by Tensorflow Hub, for even greater classification accuracy.

407 Recognizing the capabilities of the CRF as a discriminative classification algorithm given a set
 408 of sparse labels, we propose a pixel-wise semantic segmentation algorithm based upon DCNN-
 409 estimated regions of images in combination with the fully-connected CRF. This hybrid DCNN-CRF

410 approach to semantic segmentation is offered as a simpler alternative to so-called 'fully
411 convolutional' DCNNs [8,39,72] which, in order to achieve accurate pixel level classifications, require
412 much larger, more sophisticated DCNN architectures [37], which are often computationally more
413 demanding to train. Since pooling within the DCNN results in a significant loss of spatial resolution,
414 these architectures require an additional set of convolutional layers that learn the 'upsampling' between
415 the last pooling layer, which will be significantly smaller than the input image, and the pixelwise
416 labelling at the required finer resolution. This process is imperfect, therefore label images appear
417 coarse at object/label boundaries [72] and some post-processing algorithm, such as a CRF or similar
418 approach, is required to refine predictions. Because of this, we suggest that our hybrid approach
419 might be a simpler approach to semantic segmentation, especially for rapid prototyping (as discussed
420 above) and in the cases where the scales of spatially continuous features are larger than the tile size
421 used in the DCNN (Figure 9). However, for spatially isolated features, especially those that exist over
422 small spatially contiguous areas, the more complicated fully convolutional approach to pixelwise
423 classification might be necessary.

424 The CRF is designed to classify (or in some instances, where some unary potentials are
425 considered improbable by the CRF model, reclassify) pixels based on both the color/brightness and
426 the proximity of nearby pixels with the same label. We found that, typically, the CRF algorithm
427 requires DCNN-derived unary potentials, regularly spaced, for at least one quarter of pixels in
428 relatively simple scenes and about one half in relatively complicated scenes (e.g. Figure 10B) for
429 satisfactory pixelwise classifications (e.g. Figure 10C). With standardized parameter values not fine-
430 tuned to individual images or datasets, CRF performance was mixed, especially for relatively small
431 objects/features (Table 3). This is exemplified by Figure 10, in which several small outcropping rocks
432 whose pixel labels were not included as CRF unary potentials, were either correctly or incorrectly
433 labeled by the CRF, despite the similarity in their location, size, color, and their relative proximity to
434 correctly labeled unary potentials. We found that optimizing CRF parameters to reduce such
435 misclassifications could be done for an individual image, but not in a systematic way that would
436 improve similar misclassifications in other images. Whereas here we have used RGB imagery, the
437 CRF would work in much the same way with larger multivariate datasets such as multispectral or
438 hyperspectral imagery, or other raster stacks consisting of information on coincident spatial grids.

439 If DCNN-based image classification is to gain wider application and acceptance within the
440 geoscience community, demonstrable successes such as presented in this paper, need to be coupled
441 with accessible tools and datasets in order to develop deep neural network architectures to better
442 discriminate landforms and land uses in landscape imagery. To that end, we invite interested readers
443 to use our data and code (see Acknowledgements) to explore variation in classifications among
444 multiple DCNN architectures, and to use our extensive pixel-level label dataset to evaluate and
445 facilitate in the development of custom DCNN models for specific classification tasks in the
446 geosciences.
447



448

449 **Figure 10.** Classification of a typical CCR image: (A) Original image; (B) DCNN predictions; (C) CRF
 450 predictions; (D) and (E) show the same region (magnification x2) from the DCNN and CRF labels,
 451 respectively. The colored ellipses in (D) indicate small rocky areas either misclassified (red ellipses)
 452 or correctly classified (green ellipses).

453 5. Conclusions

454 Our work demonstrates the general effectiveness of a repurposed, small, very fast, existing
 455 DCNN framework called MobileNetV2 for classification of landforms, land use, and land cover
 456 features in both satellite and high-vantage, oblique and nadir imagery collected using planes, UAVs
 457 and static monitoring cameras. With no fine tuning of model parameters, we achieve average
 458 classification accuracies of between 91 and 98% (F1 scores) across five disparate datasets, ranging
 459 between 71 and 99% accuracies over 26 individual land cover/use classes across four datasets.
 460 Further, we demonstrate how structured prediction using a fully connected CRF can be used in a
 461 semi-supervised manner to very efficiently generate ground truth label imagery and DCNN training
 462 libraries. Finally, we propose a hybrid method for accurate semantic segmentation of imagery of
 463 natural landscapes based on combining 1) the recognition capacity of DCNNs to classify small
 464 regions in imagery, and 2) the fine grained localization of fully connected CRFs for pixel-level
 465 classification. Where land cover/uses that are typically much greater in size than a 96x96 pixel tile,
 466 average pixelwise F1 scores range from 86 to 90%. Smaller, and more isolated features have greater
 467 pixelwise accuracies. This is in part due to our usage of a common set of model parameters for all
 468 data sets, however further refinement of this technique may be required to classify features that are
 469 much smaller than a 96x96 pixel tile with similar accuracies as larger features and land covers.

470 These techniques should find numerous application in the classification of remotely sensed
 471 imagery for geomorphic and natural hazards studies, especially for rapidly evaluating the general
 472 utility of DCNNs for a specific classification task, and especially for relatively large and spatially
 473 extensive land cover types. All of our data, trained models, and processing scripts are available at
 474 https://github.com/dbuscombe-usgs/dl_landscapes_paper.

475 **Supplementary Materials:** The following are available online at www.mdpi.com/xxx/s1, Figure S1: Datasets,
 476 Figure S2: Confusion matrices.

477 **Author Contributions:** Conceptualization, D.B., and A.R.; Methodology, D.B., and A.R.; Software, D.B.;
 478 Validation, D.B.; Formal Analysis, D.B.; Data Curation, D.B.; Writing-Original Draft Preparation, D.B. and A.R.;
 479 Writing-Review & Editing, D.B. and A.R.; Visualization, D.B.; Funding Acquisition, D.B.

480 **Funding:** This research was funded by the U.S. Geological Survey Coastal and Marine Geology Program.

481 **Acknowledgments:** Thanks to Jon Warrick, Paul Grams and Chris Sherwood for data and discussions. Images
482 from the California Coastal Records Project are Copyright (C) 2002-2018 Kenneth & Gabrielle Adelman,
483 www.Californiacoastline.org.

484 **Conflicts of Interest:** The authors declare no conflict of interest.

485 Appendix A

486 **Table A1.** Classes and number of tiles used for the Seabright dataset.

Class	Number of training tiles (T=96/224)	Number of evaluation tiles (T=96/224)
Anthropogenic	23,566 / 4,548	15,575 / 3,031
Road and pavement	314 / 60	525 / 103
Sand	38,250 / 6,887	25,318 / 5,802
Vegetation	386 / 76	240 / 38
Other terrain	77 / 24	117 / 22
Water	11,394 / 1,723	14,360 / 2,251
Foam	5,076 / 735	5,139 / 843
Total:	76,063 / 14,053	61,274 / 12,090

487

488 **Table A2.** Classes and number of tiles used for the Lake Ontario dataset.

Class	Number of training tiles (T=96/224)	Number of evaluation tiles (T=96/224)
Anthropogenic/buildings	467 / 219	3,216 / 333
Sediment	2,856 / 289	3,758 / 407
Vegetation	33,871 / 5,139	33,421 / 5,001
Other terrain	1,596 / 157	1,094 / 92
Water	80,304 / 13,332	77,571 / 12,950
Total:	119,094 / 19,136	119,060 / 18,783

489

490 **Table A3.** Classes and number of tiles used for the Grand Canyon dataset.

Class	Number of training tiles (T=96/224)	Number of evaluation tiles (T=96/224)
Rock/scree/terrain	15,059 / 2,405	12,151 / 1,999
Sand	751 / 39	1,069 / 91
Riparian vegetation	2,971 / 408	2,158 / 305
Water	8,568 / 1,462	5,277 / 1,130
Total:	27,349 / 4,314	20,655 / 3,525

491

492 **Table A4.** Classes and number of tiles used for the California Coastal Records dataset.

Class	Number of training tiles (T=96/224)	Number of evaluation tiles (T=96/224)
Beach	39,206 / 6,460	42,616 / 7,438
Anthropogenic/buildings	34,585 / 6,904	45,831 / 8,452
Cliff	29,844 / 4,666	17,488 / 3,108
Road	6,000 / 705	3,782 / 440
Sky	41,139 / 6,694	26,240 / 4,267
Surf/foam	18,775 / 2,745	25,025 / 3,549
Swash	5,825 / 1,280	4,535 / 552
Other terrain	87,632 / 18,517	50,254 / 8,647
Vegetation	81,896 / 19,346	46,097 / 7,639
Water	121,684 / 17,123	49,427 / 11,019
Total:	466,586 / 84,440	311,295 / 55,111

493 References

- 494 1. Franklin, S.E.; Wulder, M.A. Remote sensing methods in medium spatial resolution satellite data land cover
495 classification of large areas. *Prog. Phys. Geog.* **2002**, *26*, 173-205.
- 496 2. Smith, M.J.; Pain, C.F. Applications of remote sensing in geomorphology. *Prog. Phys. Geog.* **2009**, *33*, 568-
497 582.
- 498 3. Mulder, V.L.; De Bruin, S.; Schaepman, M.E.; Mayr, T.R. The use of remote sensing in soil and terrain
499 mapping—A review. *Geoderma* **2011**, *162*, 1-19.
- 500 4. Sekovski, I.; Stecchi, F.; Mancini, F.; Del Rio, L. Image classification methods applied to shoreline extraction
501 on very high-resolution multispectral imagery. *Int. J Remote Sens* **2014**, *35*, 3556-3578.
- 502 5. Ma, L.; Li, M.; Ma, X.; Cheng, L.; Du, P.; Liu, Y. A review of supervised object-based land-cover image
503 classification. *ISPRS J. Photogramm.* **2017**, *130*, 277-293.
- 504 6. Cheng, G.; Han, J.; Lu, X. Remote sensing image scene classification: benchmark and state of the art. *P. IEEE*
505 **2017**, *105*, 1865-1883.
- 506 7. O'Connor, J.; Smith, M.J.; James, M.R. Cameras and settings for aerial surveys in the geosciences:
507 Optimising image data. *Prog. Phys. Geog.* **2017**, *41*, 325-344.
- 508 8. Long, J.; Shelhamer, E.; Darrell, T. Fully convolutional networks for semantic segmentation. *IEEE. Conf.*
509 *Comp. Vision (CVPR)* **2015**, 3431-3440.
- 510 9. Volpi, M.; Tuia, D. Dense semantic labeling of subdecimeter resolution images with convolutional neural
511 networks. *IEEE T. Geo. Remote* **2017**, *55*, 881-893.
- 512 10. Holman, R.A.; Stanley, J. The history and technical capabilities of Argus. *Coast. Eng.* **2007**, *54*, 477-491.
- 513 11. Bertoldi, W.; Zandoni, L.; Tubino, M. Assessment of morphological changes induced by flow and flood
514 pulses in a gravel bed braided river: The Tagliamento River (Italy). *Geomorphology* **2010**, *114*, 348-360.
- 515 12. Hoonhout, B.; Radermacher, M.; Baart, F.; Van der Maaten, L. An automated method for semantic
516 classification of regions in coastal images. *Coast. Eng.* **2015**, *105*, 1-12.
- 517 13. Bergsma, E.; Conley, D.; Davidson, M.; O'Hare, T. Video-based nearshore bathymetry estimation in macro-
518 tidal environments. *Mar. Geol.* **2016**, *374*, 31-41.
- 519 14. Almar, R.; Larnier, S.; Castelle, B.; Scott, T. On the use of the radon transform to estimate longshore currents
520 from video imagery. *Coast. Eng.* **2016**, *114*, 301-308.
- 521 15. Benacchio, V.; Piégay, H.; Buffin-Bélanger, T.; Vaudor, L. A new methodology for monitoring wood fluxes
522 in rivers using a ground camera: Potential and limits. *Geomorphology* **2017**, *279*, 44-58.
- 523 16. Grams, P.E.; Tusso, R.B.; Buscombe, D. Automated remote cameras for monitoring alluvial sandbars on the
524 Colorado River in Grand Canyon, Arizona. *U.S.G.S. Open File Report* **2018**, No. 2018-1019.
- 525 17. Turner, I.L.; Harley, M.D.; Drummond, C.D. UAVs for coastal surveying. *Coast. Eng.* **2016**, *114*, 19-24.
- 526 18. Su, L.; Gibeaut, J. Using UAS hyperspatial RGB imagery for identifying beach zones along the south Texas
527 coast. *Remote Sens.* **2017**, *9*, 159.

- 528 19. Sturdivant, E.J.; Lentz, E.E.; Thieler, E.R.; Farris, A.S.; Weber, K.M.; Remsen, D.P.; Miner, S.; Henderson,
529 R.E. UAS-SfM for Coastal Research: Geomorphic Feature Extraction and Land Cover Classification from
530 High-Resolution Elevation and Optical Imagery. *Remote Sens.* **2017**, *9*, p.1020.
- 531 20. Warrick, J.A.; Ritchie, A.C.; Adelman, G.; Adelman, K.; Limber, P.W. New techniques to measure cliff
532 change from historical oblique aerial photographs and structure-from-motion photogrammetry. *J. Coastal*
533 *Res.* **2016**, *33*, 39–55.
- 534 21. Fonstad, M.A.; Dietrich, J.T.; Courville, B.C.; Jensen, J.L.; Carbonneau, P.E. Topographic structure from
535 motion: A new development in photogrammetric measurement. *Earth Surf. Proc. Land.* **2013**, *38*, 421–430.
- 536 22. Javernick, L.; Brasington, J.; Caruso, B. Modeling the topography of shallow braided rivers using Structure-
537 from-Motion photogrammetry. *Geomorphology* **2014**, *213*, 166–182.
- 538 23. Woodget, A.S.; Austrums, R. Subaerial gravel size measurement using topographic data derived from a
539 UAV-SfM approach. *Earth Surf. Proc. Land.* **2017**, *42*, 1434–1443.
- 540 24. Carbonneau, P.E.; Bizzi, S.; Marchetti, G. Robotic photosieving from low-cost multicopter sUAS: A proof-of-
541 concept. *Earth Surf. Proc. Land.* **2018**.
- 542 25. Hugenholtz, C.H.; Whitehead, K.; Brown, O.W.; Barchyn, T.E.; Moorman, B.J.; LeClair, A.; Riddell, K.;
543 Hamilton, T. Geomorphological mapping with a small unmanned aircraft system (sUAS): Feature detection
544 and accuracy assessment of a photogrammetrically-derived digital terrain model. *Geomorphology* **2013**, *194*,
545 16–24.
- 546 26. Pajares, G. Overview and current status of remote sensing applications based on unmanned aerial vehicles
547 (UAVs). *Photogramm. Eng. Rem. S.* **2015**, *81*, 281–329.
- 548 27. Xie, Y.; Sha, Z.; Yu, M. Remote sensing imagery in vegetation mapping: a review. *J. Plant Ecol.* **2008**, *1*, 9–23.
- 549 28. Adam, E.; Mutanga, O.; Rugege, D. Multispectral and hyperspectral remote sensing for identification and
550 mapping of wetland vegetation: a review. *Wetl. Ecol. Manag.* **2010**, *18*, 281–296.
- 551 29. Dugdale, S.J.; Bergeron, N.E.; St-Hilaire, A. Spatial distribution of thermal refuges analysed in relation to
552 riverscape hydromorphology using airborne thermal infrared imagery. *Remote Sens. Environ.* **2015**, *160*, 43–
553 55.
- 554 30. Tamminga, A.; Hugenholtz, C.; Eaton, B.; Lapointe, M. Hyperspatial remote sensing of channel reach
555 morphology and hydraulic fish habitat using an unmanned aerial vehicle (UAV): a first assessment in the
556 context of river research and management. *River Res. Appl.* **2015**, *31*, 379–391.
- 557 31. Bryant, R.G.; Gilvear, D.J. Quantifying geomorphic and riparian land cover changes either side of a large
558 flood event using airborne remote sensing: River Tay, Scotland. *Geomorphology* **1999**, *29*, 307–321.
- 559 32. East, A.E.; Pess, G.R.; Bountry, J.A.; Magirl, C.S.; Ritchie, A.C.; Logan, J.B.; Randle, T.J.; Mastin, M.C.;
560 Minear, J.T.; Duda, J.J.; Liermann, M.C.; McHenry, M.L.; Beechie, T.J.; Shafroth, P.B. Large-scale dam
561 removal on the Elwha River, Washington, USA: River channel and floodplain geomorphic change:
562 *Geomorphology* **2015**, *228*, 765–786, doi: 10.1016/j.geomorph.2014.08.028.
- 563 33. Warrick, J.A.; Bountry, J.A.; East, A.E.; Magirl, C.S.; Randle, T.J.; Gelfenbaum, G.; Ritchie, A.C.; Pess, G.R.;
564 Leung, V.; Duda, J.J. Large-scale dam removal on the Elwha River, Washington, USA: Source-to-sink
565 sediment budget and synthesis: *Geomorphology* **2015**, *246*, 729–750, doi: 10.1016/j.geomorph.2015.01.010.
- 566 34. LeCun, Y.; Bengio, Y.; Hinton, G. Deep learning. *Nature* **2015**, *521*(7553), 436.
- 567 35. Goodfellow, I.; Bengio, Y.; Courville, A.; Bengio, Y., 2016. Deep learning (Vol. 1). Cambridge: MIT press.
- 568 36. Szegedy, C.; Ioffe, S.; Vanhoucke, V.; Alemi, A.A. Inception-v4, inception-resnet and the impact of residual
569 connections on learning. *AAAI* **2017**, *4*, 12.
- 570 37. Chen, L.C.; Papandreou, G.; Kokkinos, I.; Murphy, K.; Yuille, A.L. Deeplab: Semantic image segmentation
571 with deep convolutional nets, atrous convolution, and fully connected crfs. *IEEE T. Pattern Anal.* **2018**, *40*,
572 834–848.
- 573 38. Litjens, G.; Kooi, T.; Bejnordi, B.E.; Setio, A.A.A.; Ciompi, F.; Ghafoorian, M.; van der Laak, J.A.; van
574 Ginneken, B.; Sánchez, C.I. A survey on deep learning in medical image analysis. *Med. Image Anal.* **2017**, *42*,
575 60–88.
- 576 39. Maggiori, E.; Tarabalka, Y.; Charpiat, G.; Alliez, P. Convolutional neural networks for large-scale remote-
577 sensing image classification. *IEEE T. Geo. Remote* **2017**, *55*, 645–657.
- 578 40. Belgiu, M.; Drăguț, L. Random forest in remote sensing: A review of applications and future directions.
579 *ISPRS J. Photogramm.* **2016**, *114*, 24–31.
- 580 41. Dauphin, Y.N.; Pascanu, R.; Gulcehre, C.; Cho, K.; Ganguli, S.; Bengio, Y. Identifying and attacking the
581 saddle point problem in high-dimensional non-convex optimization. *Adv. Neur. In. (NIPS)* **2014**, 2933–2941.

- 582 42. Garcia-Garcia, A.; Orts-Escolano, S.; Oprea, S.; Villena-Martinez, V.; Garcia-Rodriguez, J. A review on deep
583 learning techniques applied to semantic segmentation. *arXiv preprint arXiv:1704.06857*, 2017.
- 584 43. Deng, J.; Dong, W.; Socher, R.; Li, L.J.; Li, K.; Fei-Fei, L. Imagenet: A large-scale hierarchical image database.
585 *IEEE. Conf. Comp. Vision (CVPR)* **2009**, 248-255
- 586 44. Russakovsky, O.; Deng, J.; Su, H.; Krause, J.; Satheesh, S.; Ma, S.; Huang, Z.; Karpathy, A.; Khosla, A.;
587 Bernstein, M.; Berg, A.C.; Fei-Fei, L. ImageNet Large Scale Visual Recognition Challenge. *IJCV*, **2015**.
- 588 45. Hu, F.; Xia, G.S.; Hu, J.; Zhang, L. Transferring deep convolutional neural networks for the scene
589 classification of high-resolution remote sensing imagery. *Remote Sens.* **2015**, *7*, 14680-14707. 8-56.
- 590 46. Långkvist, M.; Kiselev, A.; Alirezaie, M.; Loutfi, A. Classification and Segmentation of Satellite
591 Orthoimagery Using Convolutional Neural Networks. *Remote Sens.* **2016**, *8*, 329.
- 592 47. Palafox, L.F.; Hamilton, C.W.; Scheidt, S.P.; Alvarez, A.M. Automated detection of geological landforms on
593 Mars using Convolutional Neural Networks. *Comput. Geo.* **2017**, *101*, 4
- 594 48. Lu, H.; Fu, X.; Liu, C.; Li, L.G.; He, Y.X.; Li, N.W. Cultivated land information extraction in UAV imagery
595 based on deep convolutional neural network and transfer learning. *J. MT Sci.* **2017**, *14*, 731-741.
- 596 49. Marmanis, D.; Datcu, M.; Esch, T.; Stilla, U. Deep Learning Earth Observation Classification Using
597 ImageNet Pretrained Networks. *IEEE Geosci. Remote Sens. Lett.* **2016**, *13*, 105-109.
- 598 50. Sutton, C.; McCallum, A. An introduction to conditional random fields for relational learning (Vol. 2).
599 Introduction to statistical relational learning. MIT Press, 2006.
- 600 51. Lafferty, J.; McCallum, A.; Pereira, F. Conditional random fields: Probabilistic models for segmenting and
601 labeling sequence data. *Int. Conf. Mach. Learn. (ICML)* **2001**, 282–289.
- 602 52. Kumar, S.; Hebert, M. Discriminative random fields. *Int. J. Comput. Vision* **2006**, *68*, 179–201.
- 603 53. Tappen, M.; Liu, C.; Adelson, E.; Freeman, W. Learning Gaussian conditional random fields for low-level
604 vision. *IEEE. Conf. Comp. Vision (CVPR)* **2007**, 1–8.
- 605 54. Krahenbuhl, P.; Koltun, V. Efficient inference in fully connected CRFs with Gaussian edge potentials. *Adv.*
606 *Neur. In. (NIPS)* **2011**, 109–117.
- 607 55. Zhu, H.; Meng, F.; Cai, J.; Lu, S. Beyond pixels: A comprehensive survey from bottom-up to semantic image
608 segmentation and cosegmentation. *J. Vis. Commun. Image R.* **2016**, *34*, 12–27.
- 609 56. Chen, L.C.; Yang, Y.; Wang, J.; Xu, W.; Yuille, A.L. Attention to scale: Scale-aware semantic image
610 segmentation. *IEEE. Conf. Comp. Vision (CVPR)* **2016**, 3640-3649.
- 611 57. Sandler, M.; Howard, A.; Zhu, M.; Zhmoginov, A.; Chen, L.C. Inverted Residuals and Linear Bottlenecks:
612 Mobile Networks for Classification, Detection and Segmentation. *arXiv preprint arXiv:1801.04381*. **2018**.
- 613 58. Szegedy, C.; Vanhoucke, V.; Ioffe, S.; Shlens, J.; Wojna, Z. Rethinking the inception architecture for
614 computer vision. *IEEE. Conf. Comp. Vision (CVPR)* **2016**, 2818-2826.
- 615 59. He, K.; Zhang, X.; Ren, S.; Sun, J. Deep residual learning for image recognition. *IEEE. Conf. Comp. Vision*
616 *(CVPR)* **2016**, 770-778.
- 617 60. Zoph, B.; Vasudevan, V.; Shlens, J.; Le, Q.V. Learning transferable architectures for scalable image
618 recognition. *arXiv preprint arXiv:1707.07012*. **2017**
- 619 61. Howard, A.G.; Zhu, M.; Chen, B.; Kalenichenko, D.; Wang, W.; Weyand, T.; Andreetto, M.; Adam, H..
620 Mobilenets: Efficient convolutional neural networks for mobile vision applications. *arXiv preprint*
621 *arXiv:1704.04861*. **2017**.
- 622 62. TensorFlow-Hub **2018**. Available online: <https://www.tensorflow.org/hub/modules/image> (accessed on 1
623 June 1, 2018).
- 624 63. Abadi M.; Agarwal A.; Barham P.; Brevdo E.; Chen Z.; and 35 others. TensorFlow: Large-scale machine
625 learning on heterogeneous systems. 2015. Software available online: <https://www.tensorflow.org> (accessed
626 on 1 June 1, 2018).
- 627 64. Sherwood, C.R.; Brosnahan, S.M.; Ackerman, S.D.; Borden, J.; Montgomery, E.T.; Pendleton, E.A.;
628 Sturdivant, E.J. Aerial imagery and photogrammetric products from unmanned aerial systems (UAS)
629 flights over the Lake Ontario shoreline at Braddock Bay, New York, July 10 to 11, 2017. *U.S.G.S. Data Release*
630 **2018**. Available online: <https://doi.org/10.5066/F74F1PX3>.
- 631 65. California Coastal Records Project (CCRP), **2018**. Available online: <http://www.californiacoastline.org/>
632 (accessed on 1 June 1, 2018).
- 633 66. Krizhevsky, A.; Sutskever, I.; Hinton, G.E. Imagenet classification with deep convolutional neural
634 networks. *Adv. Neur. In. (NIPS)* **2012**, 1097-1105.

- 635 67. Simonyan, K.; Zisserman, A. Very deep convolutional networks for large-scale image recognition. *Proc. Int.*
636 *Conf. Learn. Represent.*, **2015**, 1-13.
- 637 68. Szegedy, C.; Liu, W.; Jia, Y.; Sermanet, P.; Reed, S.; Anguelov, D.; Erhan, D.; Vanhoucke, V.; Rabinovich, A.
638 Going deeper with convolutions. *IEEE. Conf. Comp. Vision (CVPR)*, **2015**, 1-9.
- 639 69. Castelluccio, M.; Poggi, G.; Sansone, C.; Verdoliva, L. Land use classification in remote sensing images by
640 convolutional neural networks. arXiv preprint arXiv:1508.00092. **2015**.
- 641 70. Li, X.; Shao, G. Object-based land-cover mapping with high resolution aerial photography at a county scale
642 in midwestern USA. *Remote Sens.* **2014**, *6*, 11372–11390.
- 643 71. Thomas, N.; Hendrix, C.; Congalton, R.G. A comparison of urban mapping methods using high-resolution
644 digital imagery. *Photogramm. Eng. Remote Sens.* **2003**, *69*, 963–972.
- 645 72. Fu, G.; Liu, C.; Zhou, R.; Sun, T.; Zhang, Q. Classification for high resolution remote sensing imagery using
646 a fully convolutional network. *Remote Sens.* **2017**, *9*, 498.
- 647



© 2018 by the authors. Submitted for possible open access publication under the terms and conditions of the Creative Commons Attribution (CC BY) license

650 (<http://creativecommons.org/licenses/by/4.0/>).